Chapter 3

Chapter 3

Bandgap engineered multi-junction photocatalyst for enhanced visible-light-driven degradation of organic pollutants

The development of heterojunctions between distinct semiconductors is regarded as an effective strategy to inhibit the recombination of photogenerated charge carriers by facilitating rapid electron-hole separation across the interfacial junction. In this chapter, titanium dioxide (TiO_2) is chosen as the host material due to its high stability and strong redox capability, and it is incorporated with cobalt (Co) to form a Co-doped $TiO_2/CoTiO_3$ heterostructure photocatalyst. The goal is to enable visible light absorption in the photocatalyst by reducing the bandgap of the host semiconductor with doping, while concurrently reducing charge carrier recombination and promoting efficient charge separation via heterojunction formation. These synergistic modifications create a favorable environment for improved visible-light-driven photocatalysis, as demonstrated in this chapter. Thus, a Co-doped $TiO_2/CoTiO_3$ heterostructure photocatalyst was synthesized using a facile and cost-effective modified sol-gel route. The XRD analysis of the photocatalyst reveals the presence of anatase-rutile homojunction and the high crystallinity nature of TiO_2. The spectral response and the bandgap of the photocatalysts were analyzed using UV-DRS. The decrease in bandgap due to Co ion doping, as well as the synergistic effect of both homojunction and heterojunction in Co-$TiO_2/CoTiO_3$, significantly enhances the photocatalytic activity under visible light. The presence of oxygen vacancies, charge carrier migration, and the chemical compositions of the photocatalysts were studied using ESR, PL, and XPS techniques. The work presented in this chapter aligns with the two primary objectives of this thesis, namely addressing the challenges of high charge carrier recombination and the inherently wide bandgap of the photocatalyst.

3.1. Introduction

The transition metal doping on the host semiconductor can increase the spectral response and reduce the recombination rate [1-3]. Cobalt is regarded as one of the most promising transition metal dopants for enhancing the visible light response of a host semiconductor. Liu et al. reported efficient photoelectrochemical (PEC) water splitting by Co-doped TiO_2 nanowire arrays integrated on a fluorine-doped tin oxide (FTO) substrate [4]. Mragui et al. demonstrated excellent methyl orange (MO) conversion

using 1% Co-doped TiO_2 under visible light [5]. However, highly concentrated transition metal doping often suffers from major setbacks such as thermal instability and poor quantum yield of the photocatalytic reactions [6]. The fabrication of a heterojunction between different photocatalytic materials is considered a viable method to suppress the photogenerated charge recombination that occurs during swift electron–hole separation through the interfacial junction [7, 8]. The built-in electric field due to the energy band mismatch across the junctions promotes the photogenerated charge carrier separation [7]. Zhang et al. demonstrated substantial charge carrier separation and significant visible light response in an n-p-n type heterojunction of TiO_2@Bi_2O_3@TiO_2 [9]. Coupling TiO_2 with low-bandgap titanium-based typical $ATiO_3$ structured perovskite materials (A = Fe, Pb, Zn, Co, Sr, and Ni) has drawn significant attention due to their excellent photocatalytic degradation [10-12]. The improved interfacial charge transfers in the perovskite ABO_3 material within the localized electric field caused by the spontaneous dipole moment enhance the photocatalytic activity [12]. Cobalt titanate ($CoTiO_3$) is a narrow-bandgap perovskite oxide material studied for potential applications in magnetic media, electronic noses, and Li-ion batteries [13, 14]. Again, $CoTiO_3$ has been reported with high photocatalytic degradation and oxygen evolution activity [15, 16]. Recently, Lin et al. reported a visible-light-active Type II heterojunction between C-TiO_2 and $CoTiO_3$ exhibiting effective photoactivity and remarkable reusability in the degradation of ciprofloxacin [17]. Noypha et al. reported a Fe_2O_3-graphene-Ag catalyst that can undergo sonocatalytic activity toward MB [18]. Again, a self-recoverable ZnS-WO_3-$CoFe_2O_4$ nanohybrid photocatalyst was illustrated by the Palanisamy research group; however, their photocatalytic efficiency toward MB was relatively lower than that achieved in this chapter [19]. In the present chapter, cobalt-doped titania (Co-TiO_2) was synthesized using a cost-effective sol-gel route. Subsequently, Co-TiO_2/$CoTiO_3$ heterojunction with TiO_2 mixed-phase (anatase-rutile) homojunction was attained via a post-thermal treatment. A $CoTiO_3$ perovskite structure was confirmed along with the mixed polymorphs of TiO_2 using various characterization techniques. The coexistence of $CoTiO_3$ and Co-TiO_2 matrix had a synergistic role in enhancing photocatalytic activity under visible light toward MB degradation.

3.2. Experimental details

3.2.1. Materials and methods

The Co-doped TiO_2 nanoparticles were prepared using titanium (IV) isopropoxide (TTIP, 95%, Alfa Aesar, USA), 2-propanol (99%, Merck, India), cobalt (II) nitrate ($Co(NO_3)_2.6H_2O$, 97%, Merck, India) and nitric acid (HNO_3, 69%, Merck, India). Initially, a precursor solution was prepared with 40 mL of 2-propanol and 4 mL of TTIP. Subsequently, a specific amount (1 wt% Co) of cobalt compound was mixed with the precursor solution. An hour later, 1 mL of HNO_3 was poured into the mixture. The solution was then stirred vigorously for the following 24 h and kept for aging till the next 72 h. The remaining moisture was removed by heating and the obtained product was then pulverized into fine powder. The obtained sample was then annealed at 400, 600, and 700 ºC for two hours and denoted as CT400, CT600, and CT700. A block diagram representation of the synthesis procedure is provided in Figure 3.1.

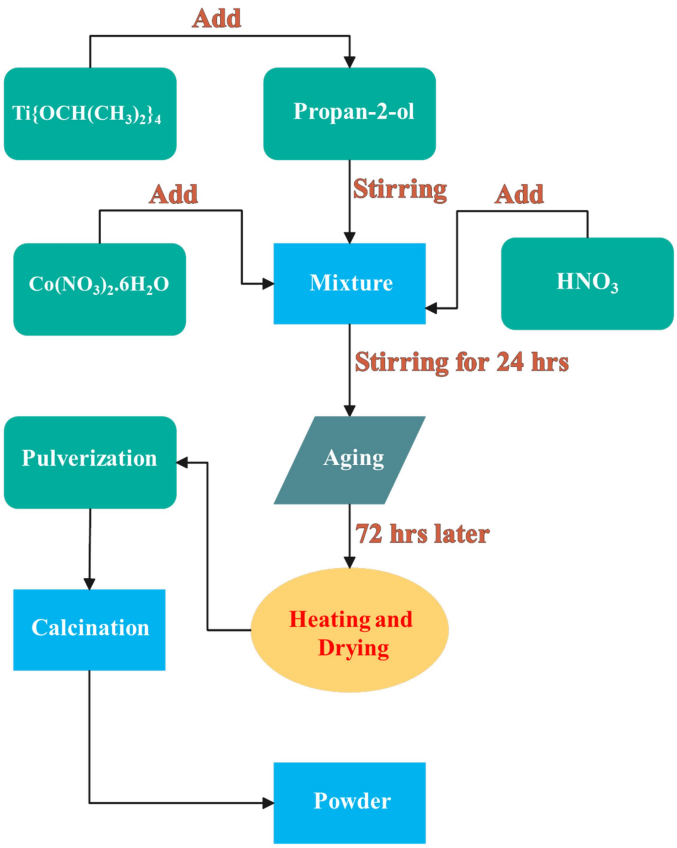

Figure 3.1. Block diagram illustrating the synthesis of Co-doped TiO_2 step by step.

For the preparation of pure TiO_2, initially, 40 mL of isopropanol was taken in a beaker and then 4 mL of TTIP was poured dropwise and homogenized. Subsequently, after 30 min, 1 mL of HNO_3 was added. This solution mixture was continuously stirred for the following 24 h and further aged for another 72 h to get a gel form. The gel was then heated to eliminate any leftover moisture before being grounded into a fine powder. The as-prepared sample was then annealed at 400 ºC and termed as a T400 photocatalyst.

3.2.2. Characterization

The photocatalysts were characterised using the following analysis techniques: XRD, UV-visible DRS, SEM, TEM, ESR, Photoluminescence and XPS. The details of the instrument for the technique have been discussed in Chapter 2. The photocatalytic performance of the photocatalysts was evaluated against MB dye degradation following the procedures as described in Chapter 2.

3.3. Results and discussion

3.3.1. XRD analysis

X-ray diffraction profiles of the photocatalysts T400, CT400, CT600, and CT700 are presented in Figure 3.2. The JCPDS reference of TiO_2 for both the anatase and rutile phases, corresponding to PDF no: 89-4921 and 89-4920 are shown in the figure. The observed peaks at $2\theta = 25.5^o$, 37.7^o, 48.1^o, 53.8^o, 55.3^o, 62.6^o, and 75.3^o in T400 and CT400 are ascribed to the anatase structure of TiO_2, which are related to the (101), (004), (200), (105), (211), (204), and (215) planes, respectively. No diffraction peak was observed for the rutile phase in the T400 and CT400. However, the peak corresponding to the rutile phase appeared at higher calcination temperatures. XRD peaks at 25.3^o, 37.7^o, 48.2^o, 53.8^o, 55.1^o, 62.6^o, 75.2^o, and $2\theta = 27.2^o$, 36.3^o, 41.1^o, 54.4^o, 56.6^o, 64.2^o, 69.1^o, 69.9^o in CT600 photocatalyst, are due to the anatase and rutile phase, respectively [20]. Their reflection planes corresponding to the rutile diffraction peaks are (110), (101), (111), (211), (220), (310), (301), and (112). On the other hand, CT700 sample exhibited only the rutile phase of TiO_2. A similar result of temperature-dependent phase transformation was obtained for pristine TiO_2 that was calcined at 600 ºC (T600) and 700 ºC (T700), and their diffraction patterns are shown in Figure 3.3. Excess interface defects at the anatase grains act as a nucleation site for the growth of the rutile phase when the calcination temperature is increased.

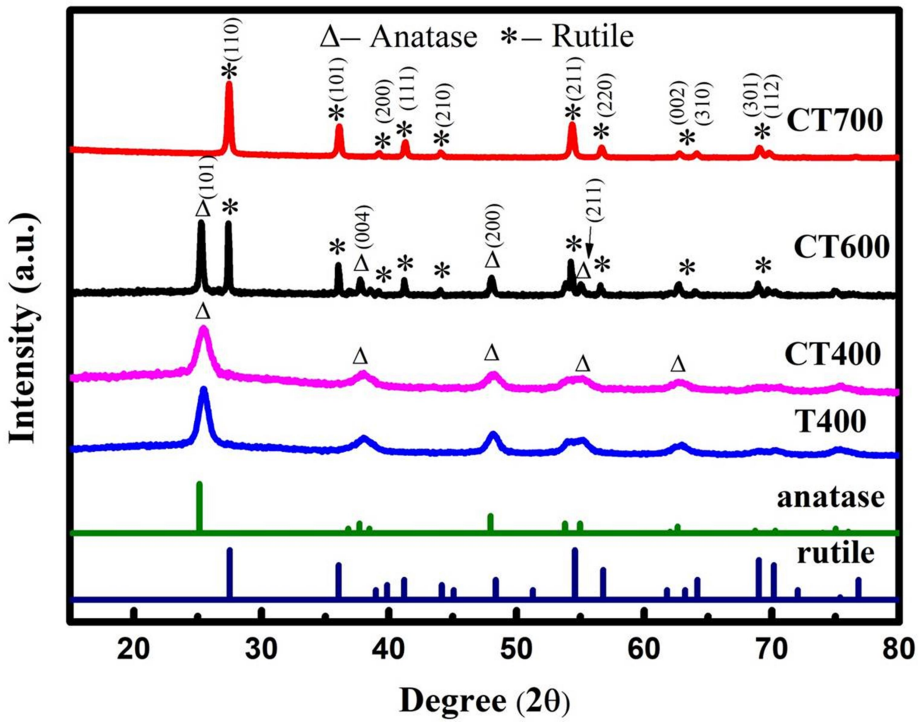

Figure 3.2. X-ray diffraction spectra of T400, CT400, CT600, and CT700.

During the calcination of anatase grains at a higher temperature, interface defects are removed, initiating a nucleation process with different atomic arrangements in the basic TiO_6 octahedra that facilitates the formation of the rutile phase [21, 22]. Thus, T600 sample shows both the phases of TiO_2, i.e. anatase and rutile phase corresponding to PDF no: 89-4921 and 89-4920, respectively. while the T700 sample exhibited only rutile phase.

XRD peak of Co and $CoTiO_3$ phase was not detected in the diffraction spectra of CT400, CT600, and CT700 due to the low doping concentration. However, diffraction peaks of the $CoTiO_3$ structure were observed on increasing the Co concentration. Figure 3.4 shows the XRD spectrum of $TiO_2/CoTiO_3$ with 20 wt% of Co (calcined at 400 ^oC). The XRD peaks due to TiO_2 (anatase) and $CoTiO_3$ phase are shown with the symbol hash (#) and asterisk (*), respectively in Figure 3.4. The diffraction peaks at $2\theta = 32.8^o$, 35.4^o, 40.5^o, 49.1^o, 61.9^o, and 63.5^o (PDF: 77-1303) were assigned to the rhombohedral structure of $CoTiO_3$.

The crystallite size of TiO_2 was calculated using Scherrer's relation (equation 2.2). The calculated *D* value of T400 and CT400 was ~11 and ~10 nm. The crystal sizes are found to increase with increasing annealing temperature (shown in Table 3.1).

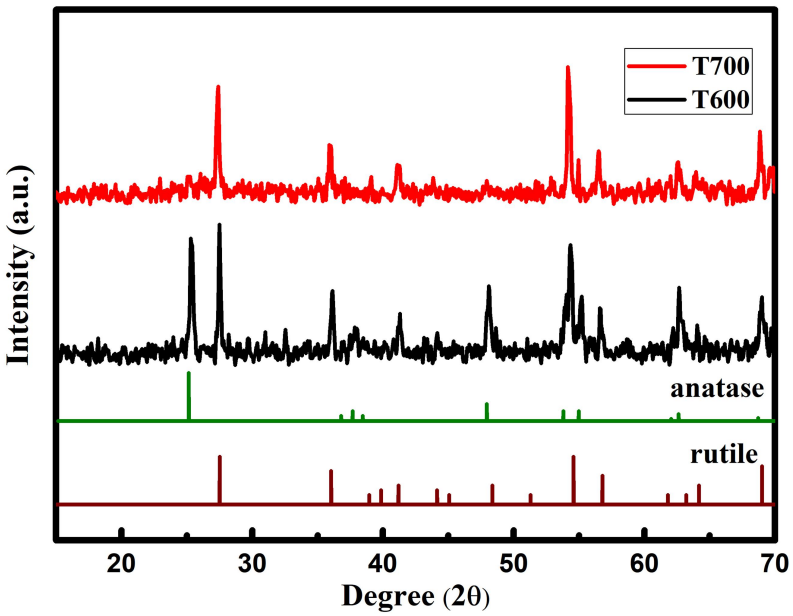

Figure 3.3. XRD spectra of pristine TiO_2 calcined at 600 °C (T600) and 700 °C (T700).

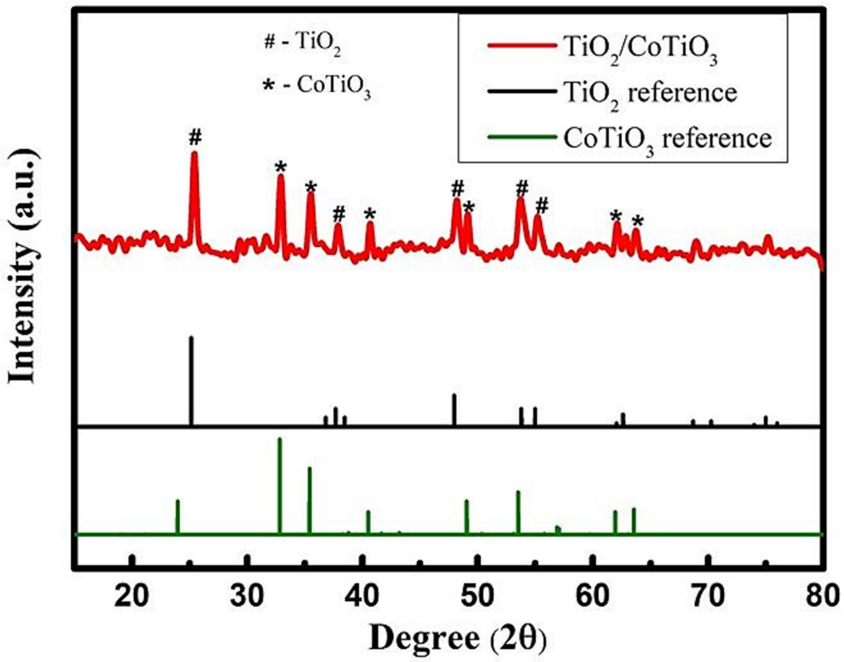

Figure 3.4. X-ray diffraction spectrum of $TiO_2/CoTiO_3$ with 20 wt% Co.

This occurs because smaller crystallites possess higher surface energy, and atomic reordering becomes significant at elevated temperatures[23]. At low temperature, smaller grains remain stable, but upon heating they coalesce into larger grains through grain boundary migration driven by atomic diffusion [24]. The increased thermal energy enables atoms to overcome potential barriers within each grain, facilitating boundary movement. During grain growth, smaller crystallites are either incorporated into larger neighboring grains or grow at their expense, as their higher surface energy makes them less stable. At sufficiently high temperature, smaller anatase grains may directly transform into rutile or first grow into larger anatase particles [24]. The smaller rutile grains then further coarsen, while larger anatase grains undergo a comparatively slower transformation into rutile [24].

3.3.2. UV-vis-DRS analysis

Absorbance spectra of T400, CT400, CT600, and CT700 in the UV-visible region are shown in Figure 3.5(a). A sharp spectral absorption corresponding to the primary energy-band transitions of TiO_2 was observed in the ultraviolet region (around 380 nm) in the pure TiO_2 [8]. The broad nature of the absorbance spectrum in Co-doped TiO_2 (CT400) with a slight red-shift compared to the pure TiO_2 (T400) was observed. The absorbance spectra were further shifted toward longer wavelengths in the CT600 and CT700. These red-shifts in the optical absorption were ascribed to the bandgap reduction as a consequence of the interaction between free sp-electrons and localized d-electrons of Co ions [25]. In addition, strong spectral absorption in the range of 500 to 750 nm was detected in both the CT600 and CT700 photocatalysts, which is related to the characteristic absorption band of the $CoTiO_3$ phase arising due to Co^{2+} to Ti^{4+} charge transfer interaction [26]. However, this wide range spectral response was decreased significantly in CT700, ascribing the dominance of the rutile structure at high calcination temperature. The bandgap values of all the materials were obtained by extrapolating the absorption band to the hυ axis from the (hυ vs. $(F(R).h\upsilon)^2$ graph (shown in Figure 3.5(b)). The graph exploits equation (2.7) as it relates the bandgap E_g of the materials with hυ. However, the value of n has to be known beforehand to plot the graph as shown in Figure 3.5(b). In this regard, n was determined by taking the logarithm of equation (2.6) [27] as follows:

$$\ln(\alpha.h\nu) = \ln A + n \ln(h\nu - E_g) \quad (3.1)$$

By plotting $\ln(h\nu - E_g)$ vs. $\ln(\alpha . h\nu)$ graph, the slope n was obtained to be ~0.5 for all the photocatalysts (shown in Figure 3.6), which suggests the direct band transition ($n = 1/2$) of the materials. As shown in Figure 3.5(b), the bandgap of the pristine T400 was found to be ~3.24 eV that concurs to the electronic transition between the primary energy bands of the anatase phase of titania. The bandgap of CT400, CT600, and CT700 photocatalysts are reduced to 3.08, 3.01, and 2.90 eV. This bandgap reduction was due to the formation of defect sites in the forbidden locality of titania by Co^{2+} ion substitution in the TiO_2 matrix [25, 28]. Notably, two additional bandgaps were obtained for each cobalt-doped titania CT400, CT600, and CT700, shown in Figure 3.5(c) (enlarged scale of Figure 3.5(b)).

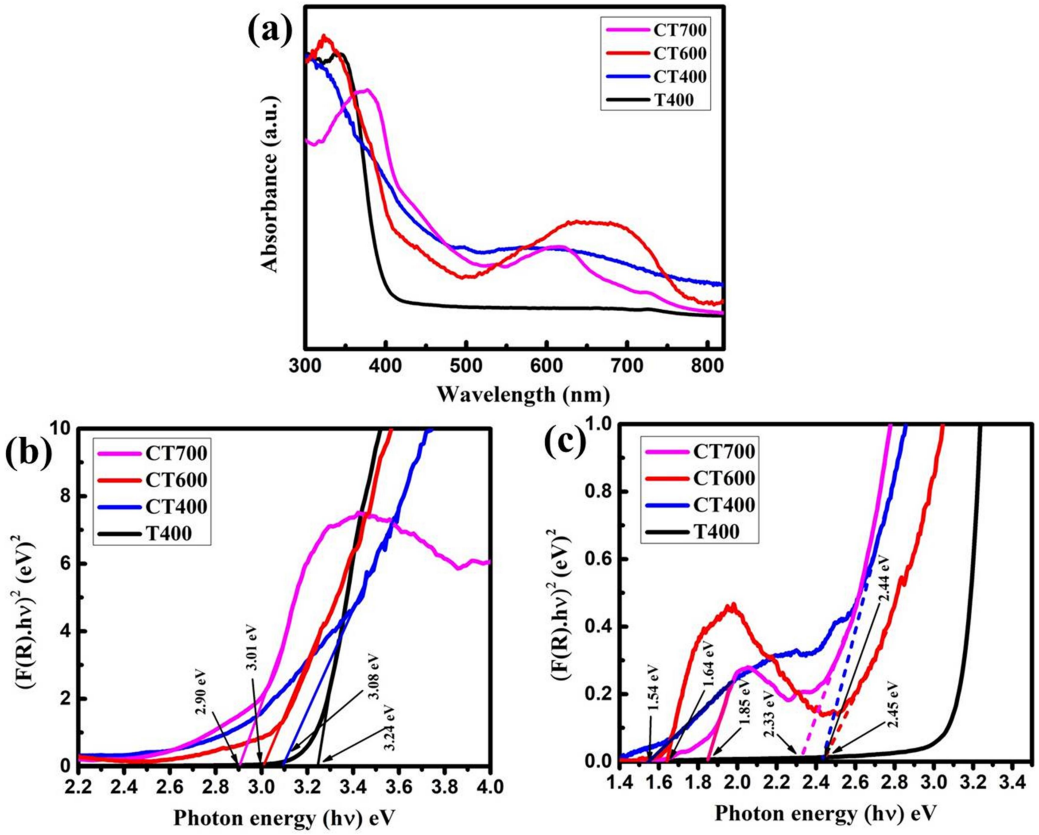

Figure 3.5. (a) Optical absorbance spectra, (b) bandgap determination, and (c) magnified y-axis data of T400, CT400, CT600, and CT700 photocatalysts.

The bandgap values are mentioned in Table 3.1. The bandgap of CT400, CT600, and CT700 was estimated to be 2.44, 2.45, and 2.33 eV, which were related to the $CoTiO_3$ phase arising due to the $Co^{2+} \rightarrow Ti^{4+}$ charge transfer (octahedral coordination Co^{2+}) [29]. Additionally, the optical transitions corresponding to the energy 1.54, 1.64, and 1.85 eV are associated with the $^4A_2(F)$ to $^4T_1(P)$ transition in the tetrahedrally coordinated Co^{2+} or Co^{3+} [25]. The above results and discussion indicate the formation of the Co-doped TiO_2 and $CoTiO_3$ phases in the matrix (Co-TiO_2/$CoTiO_3$). The narrow TiO_2 bandgap occurred due to Co doping improved visible light absorption, and the interfacial junctions minimized the recombination rate and prolonged the charge carriers for photocatalytic reactions.

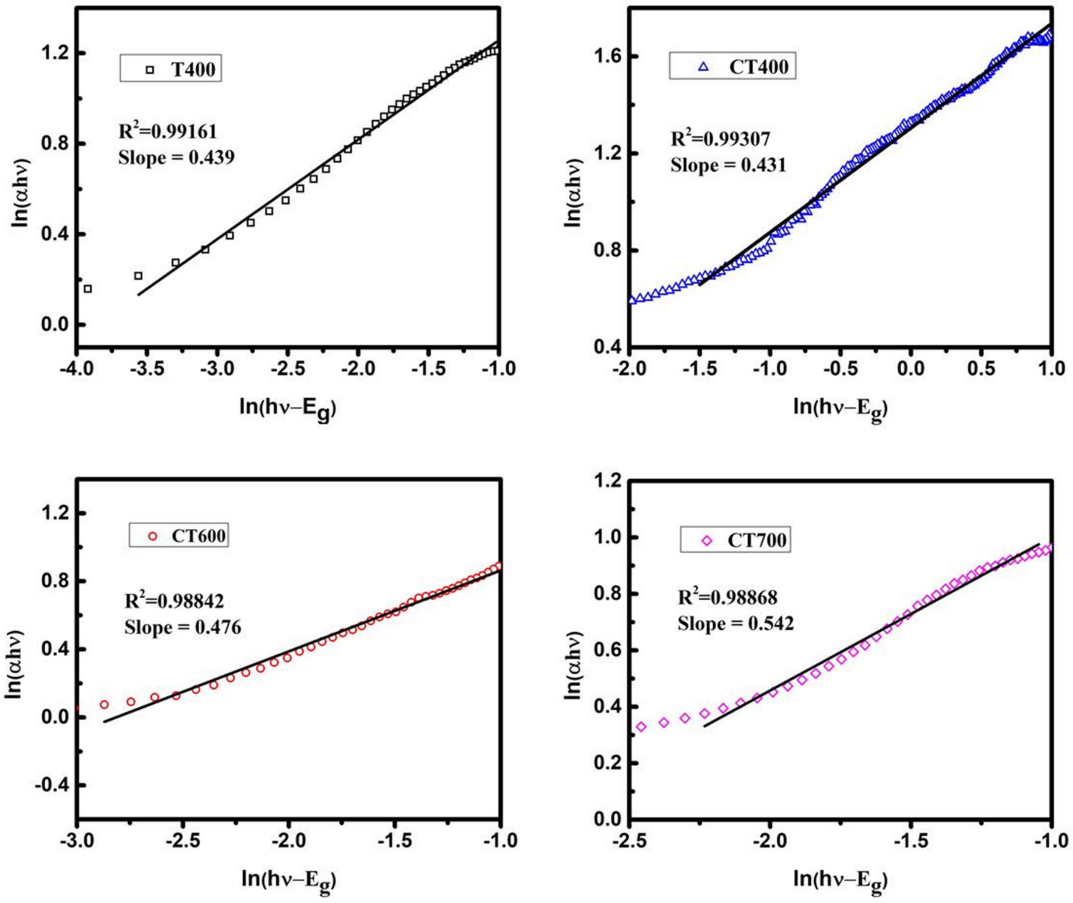

Figure 3.6. Determination of n value by plotting $\ln(\alpha.h\nu)$ vs. $\ln(h\nu - E_g)$ graph.

Table 3.1. Transitional energy and crystallite size of the as-prepared photocatalysts.

Photocatalyst	Energy of transitions (eV)	Crystallite size (nm)
T400	3.24	~11
CT400	3.08, 2.44, 1.54	~10
CT600	3.01, 2.45, 1.64	~25
CT700	2.90, 2.33, 1.85	~29

3.3.3. SEM and TEM analysis

SEM images were examined to understand the morphological structure of the photocatalysts. Figure 3.7(a) and Figure 3.7(b) depict the SEM images of pristine titania (T400) and Co-doped titania (CT600).

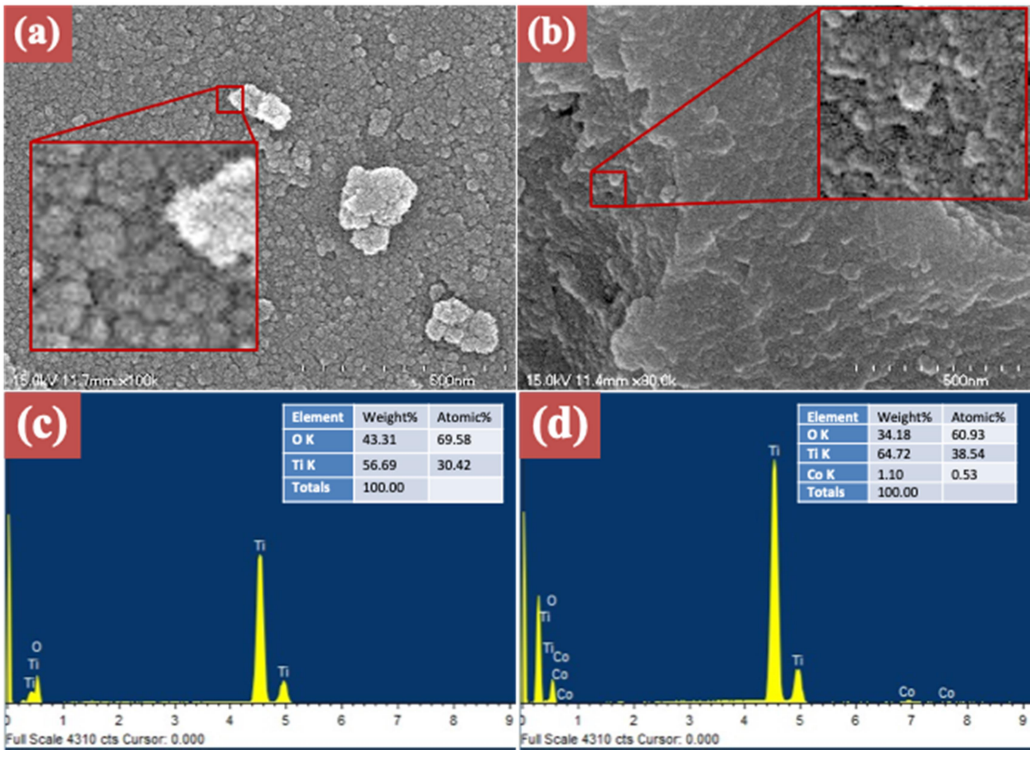

Figure 3.7. SEM images of (a) T400 and (b) CT600, along with their magnified view of the selected area. EDX of (c) T400, and (d) CT600 with atomic composition.

The homogeneous distribution was confirmed in T400 and CT600 having average particle sizes of ~20 and ~23 nm, respectively. Figure 3.7(c) and 3.7(d) represent the EDX spectra of the T400 and CT600 photocatalysts with their atomic compositions.

EDX results confirmed the existence of Ti, O, and Co in the CT600 sample. Both T400 and CT600 photocatalysts exhibited mesoporous structures with no major aggregation of larger-size clusters.

To study the particle size distribution and microstructure of the photocatalysts, the TEM and HR-TEM images were analyzed. Figure 3.8(a-b) and 3.8(c-d) depict the TEM and HR-TEM images of T400 and CT600, respectively. The particle size homogeneity in T400 and CT600 is evident in Figure 3.8(a) and 3.8(c). The interplanar *d*-spacing of T400 was calculated to be 3.4 Å, which is the typical value of the anatase phase of TiO_2 (Figure 3.8(b)). The HR-TEM image of CT600 in Figure 3.8(d) shows *d*-spacing values of 3.4 Å and 3.2 Å corresponding to the anatase and rutile phases, respectively. Additionally, CT600 exhibits an interplanar gap of d = 2.7 Å, which was attributed to the $CoTiO_3$ crystal. This result further indicates the coexistence of $CoTiO_3$ crystal in the matrix along with the anatase and rutile phases.

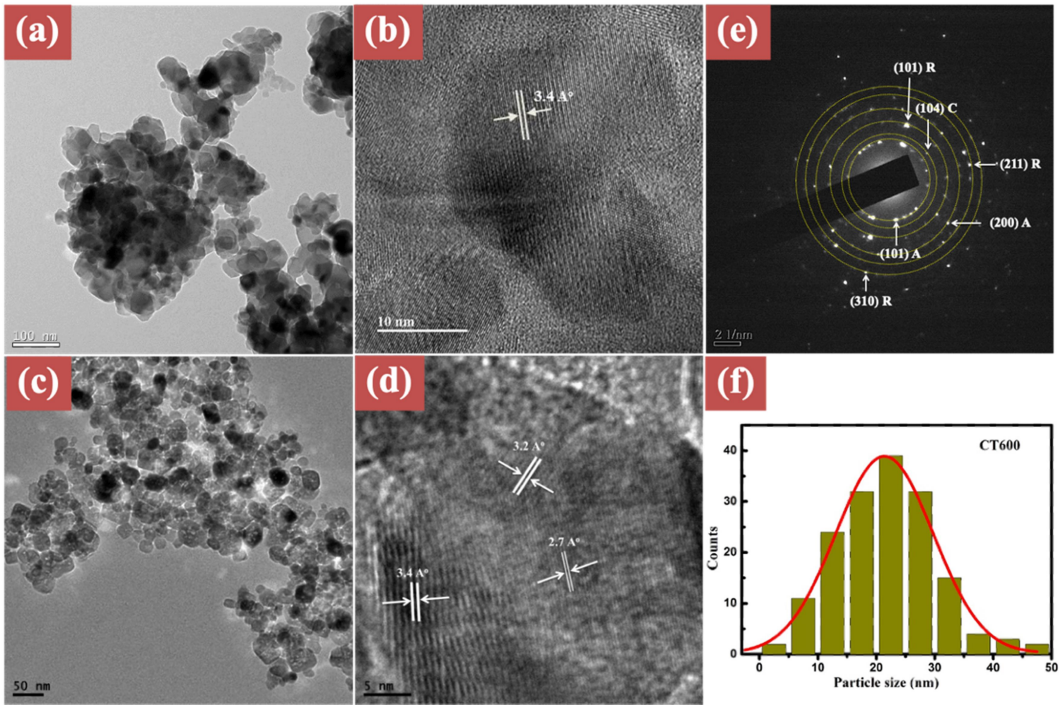

Figure 3.8. TEM and high-resolution TEM (a, b) T400 and (c, d) CT600. (e) SAED pattern with the lattice planes and (f) particle distribution of CT600.

The selected area electron diffraction (SAED) pattern of the CT600 photocatalyst is presented in Figure 3.8(e). The concentric rings reveal the polycrystalline nature of the

photocatalyst [30]. The *d*-spacing (radius calculated from the central spot of the Scherrer's ring) of the anatase phase corresponding to (101) and (200) planes agree with the calculated values from XRD. The concentric rings of (101), (211), and (310) planes are assigned to the *d*-spacings of the rutile phase. In addition, the *d*-spacing corresponding to the $CoTiO_3$ phase was indexed with the (104) designated ring. The mean particle size distribution of CT600 is illustrated in the bar diagram of Figure 3.8(f), showing a mean value of ~22 nm.

3.3.4. ESR analysis

Photocatalysts under light irradiation generate electron-hole pairs that interact with H_2O and dissolved oxygen, producing radicals such as $^{\bullet}O_2^-$, h^+, and e^-, which perform the redox reactions. The number of free electrons and oxygen vacancies within the photocatalyst can be obtained from ESR. Figure 3.9 shows the ESR results of T400, CT400, and CT600 photocatalysts measured at room temperature using microwave frequency of 9.44 GHz. The Lande *g*-factor of the electrons are calculated from $g = {}^{h\nu}/_{\beta H_o}$, where h, ν, β, and H_o represent Planck constant, frequency, Bohr magnetron, and resonance magnetic field, respectively [31]. The broad anisotropic resonance peak observed at g = 2.06 and 2.03 in T400 and CT400 is assigned to the surface Ti^{3+}, where the atmospheric O_2 gets adsorbed and consequently reduced to O^{2-} [32]. The anisotropic nature of the spectra are assigned to altered distribution of paramagnetic species in the system. The ESR peak intensity significantly increased after Co incorporation in TiO_2, indicating the formation of additional Ti^{3+} species. The ESR resonance signal at g = 2.23 in CT600 was attributed to Co^{2+} ions associated with oxygen vacancies in the octahedral sites of $CoTiO_3$ [32, 33]. Additionally, a hump in the ESR curve was seen at g = 2.51 in CT400 and g = 2.67 in CT600, which was attributed to the tetrahedrally coordinated high-spin state of Co^{2+} ions [25, 33].

3.3.5. Photoluminescence spectra analysis

Figure 3.10(a) shows the room temperature PL spectra of T400, CT400, and CT600 photocatalysts at an excitation wavelength of 320 nm. The emission peak at 385 nm in T400 is ascribed to the TiO_2 onset band transitions with a bandgap of ~3.2 eV.

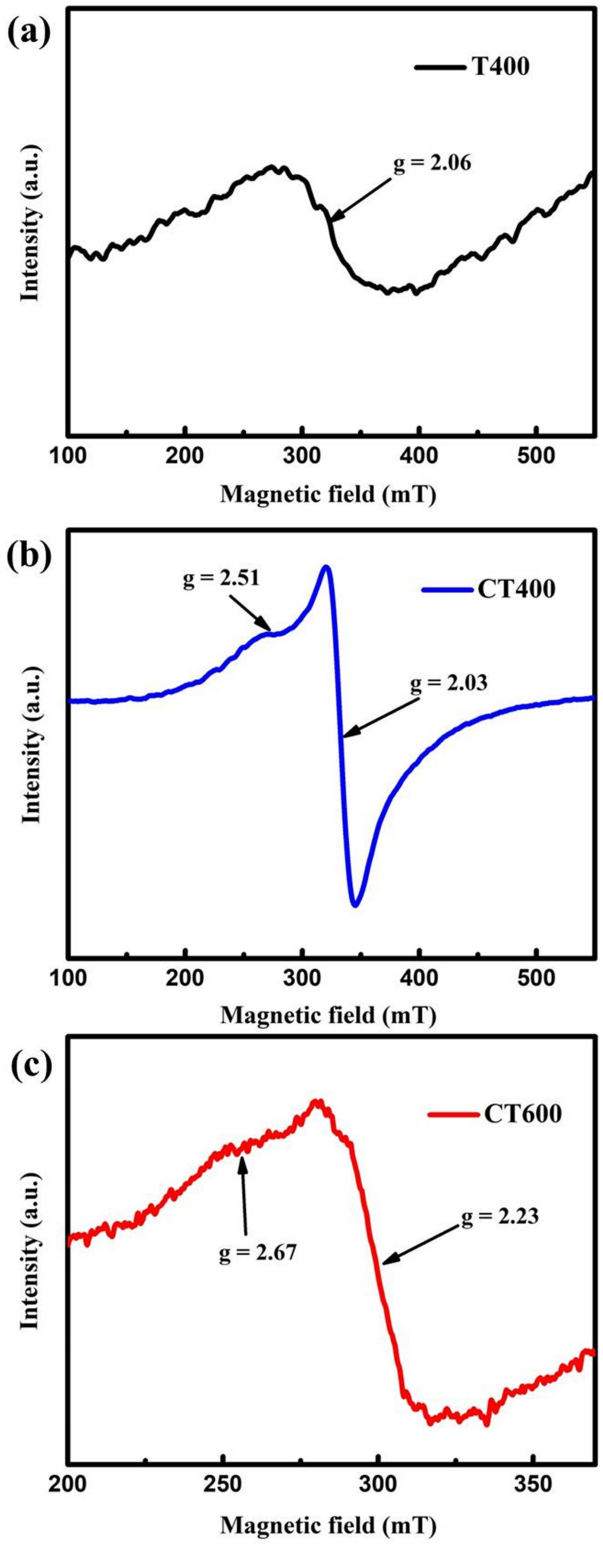

Figure 3.9. ESR spectra of (a) T400, (b) CT400, and (c) CT600 photocatalysts at room temperature.

The PL intensity was observed to be quenched in both CT400 and CT600, indicating a lower recombination rate of photogenerated charge carriers. Figure 3.10(b-d) shows the Gaussian fitting of the PL spectra of T400, CT400, and CT600 photocatalysts. The PL peaks at 440, 441 and 454 nm in CT400 and CT600 correspond to the defect state transitions due to Co^{2+} ion substitution in the TiO_2 matrix [25]. The low-intensity emission peaks at around 472 - 485 nm correspond to the self-trapped excitons generated due to the transition from Ti^{3+} 3d states to the deep acceptor levels near the valence band maximum [34, 35]. The emission at around 521 nm, corresponding to an energy gap of ~2.4 eV, originated from the transition of electrons from the lower level of oxygen vacancies to the ground state [35].

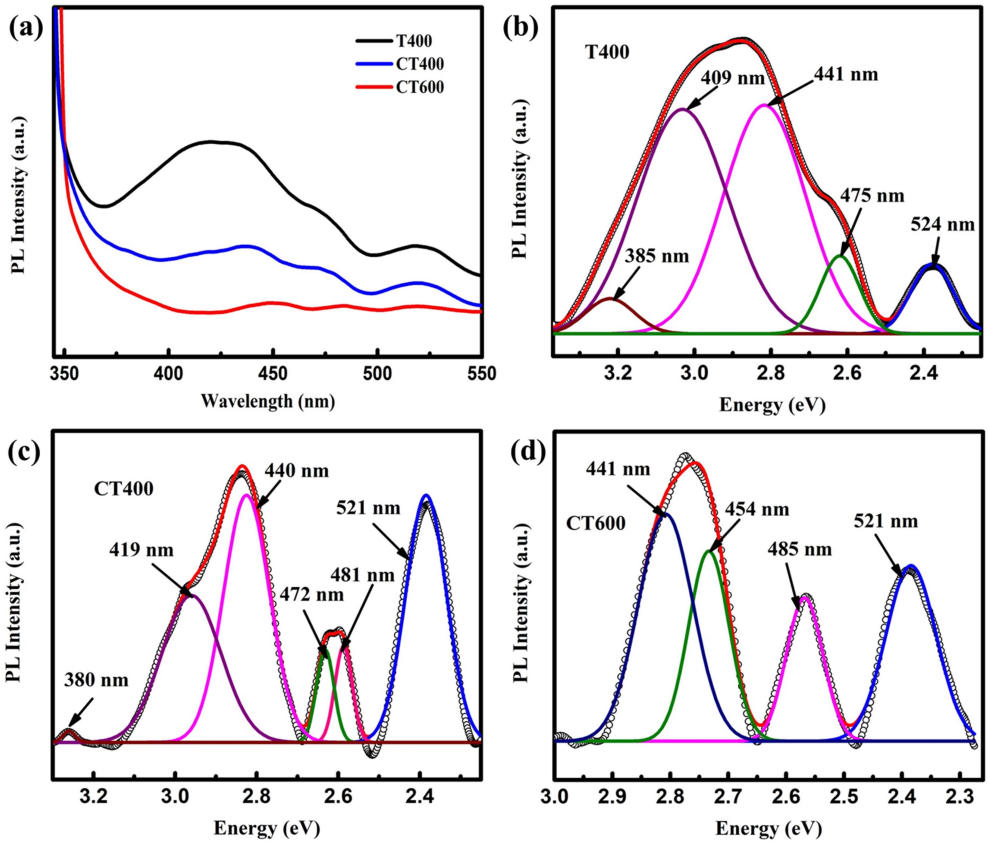

Figure 3.10. (a) Photoluminescence spectra of T400, CT400, and CT600 photocatalysts at room temperature, (b-d) Gaussian fitting of each PL spectrum of T400, CT400, and CT600.

3.3.6. XPS analysis

The oxidation state and chemical composition of the prepared photocatalyst were studied using XPS. The full survey spectra of T400, CT400, and CT600 are shown in Figure 3.11(a). The presence of Ti, O, and Co on the surface of CT400 and CT600 catalysts was confirmed. A peak attributed to extraneous carbon contamination was observed at a binding energy (BE) of 285.5 eV [36], likely arising from carbon compounds adhered to the photocatalyst surface. XPS spectra of Ti 2p and O 1s for T400, CT400, and CT600 are presented in Figure 3.11(b) and 3.11(c). The O 1s peaks are found to be slightly shifted towards higher binding energies in Co-doped TiO_2. The high-resolution Ti spectra of T400 reveal the presence of Ti^{4+} state identified with two prominent peaks at BE 458.2 and 464.0 eV, corresponding to Ti ($2p_{3/2}$) and Ti ($2p_{1/2}$) doublets [37]. After Co doping, the Ti 2p peaks are shifted towards higher BE by ~0.3 and ~0.6 eV in CT400 and CT600, respectively.

The positive shift observed in the binding energy values of O 1s peaks of CT400 and CT600 in comparison to T400 indicates lower electron density of oxygen species of TiO_2 formed in CT400 and CT600 than in T400 [38]. Again, the positive shifts observed in the binding energy values of Ti 2p peaks of CT400 and CT600 in comparison to T400 suggest the presence of higher electron density at Ti sites. This implies the existence of surface defects due to Co doping in CT400 and CT600, which in turn reduces the Fermi level [38-40]. However, the Ti 2p doublet is separated by 5.8 eV representative of the standard value of TiO_2 [41, 42]. The Ti ($2p_{3/2}$) and Ti ($2p_{1/2}$) peaks appear at 458.5 and 464.3 eV in CT400, respectively, whereas in CT600 they are shifted to 458.8 and 464.6 eV.

For T400, the Ti 2p spectrum was deconvoluted into four peaks at 457.7, 458.2, 463.5, and 464.0 eV (shown in Figure 3.12(a)). The shoulder peaks at 457.7 and 463.5 eV correspond to the Ti^{3+} ($2p_{3/2}$) and Ti^{3+} ($2p_{1/2}$), respectively. Likewise, the Ti 2p spectra of Co incorporated catalysts were deconvoluted into four peaks. They were positioned at 457.8, 458.5, 463.6, and 464.3 eV in CT400 (Figure 3.12(b)) and at 458.2, 458.8, 464.0, and 464.6 eV in CT600 (Figure 3.12(c)). The deconvoluted peaks at 457.8 and 463.6 eV in CT400, and at 458.2 and 464.0 eV in CT600, are ascribed to the Ti^{3+} $2p_{3/2}$ and Ti^{3+} $2p_{1/2}$ states, respectively [40, 43]. The XPS peak area corresponding to Ti^{3+} $2p_{3/2}$ increased by ~7% and ~21% in CT400 and CT600, respectively, compared

with the pristine T400 photocatalyst. Similarly, the peak area corresponding to Ti^{3+} $2p_{1/2}$ increased by ~47% and ~12% in CT400 and CT600, respectively, compared with pristine T400. Consequently, the area of the peaks corresponding to Ti^{4+} $2p_{1/2}$ and Ti^{4+} $2p_{3/2}$ decreased significantly in both CT400 and CT600. This indicates the generation of more oxygen vacancies after Co incorporation into TiO_2, consistent with the ESR analysis. The deconvoluted XPS peak areas of the photocatalysts are summarized in Table 3.2.

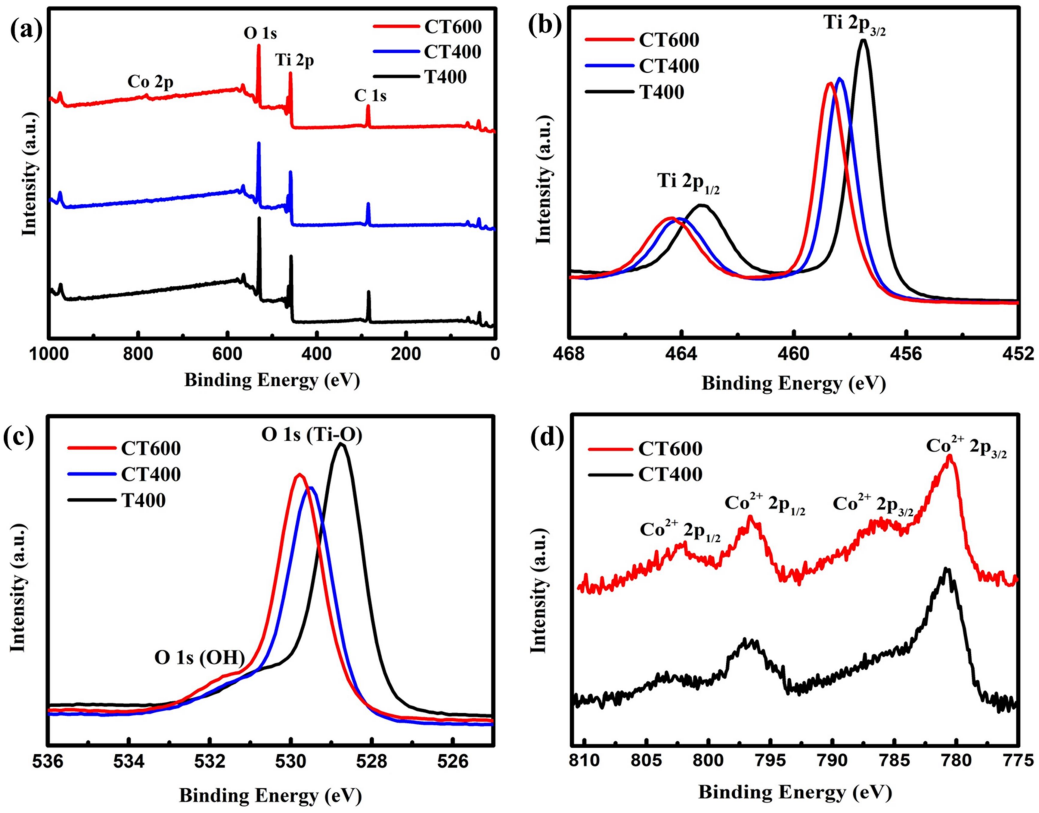

Figure 3.11. XPS spectra of T400, CT400, and CT600. (a) Full survey profile, (b) Ti 2p spectra, (c) O 1s spectra, and (d) Co 2p spectra.

The high-resolution O 1s XPS peaks of pristine TiO_2 (T400), located at binding energies (BE) of 529.2 and 531.5 eV, are imputable to the lattice-oxygen (Ti-O) and the bridging hydroxyl groups (Ti-OH) on the surface, respectively (shown in Figure 3.11(c)) [40]. A slight positive shift in the O1s peaks was observed at 529.4 and 531.7 eV for CT400; and at 529.7 and 532.0 eV for CT600.

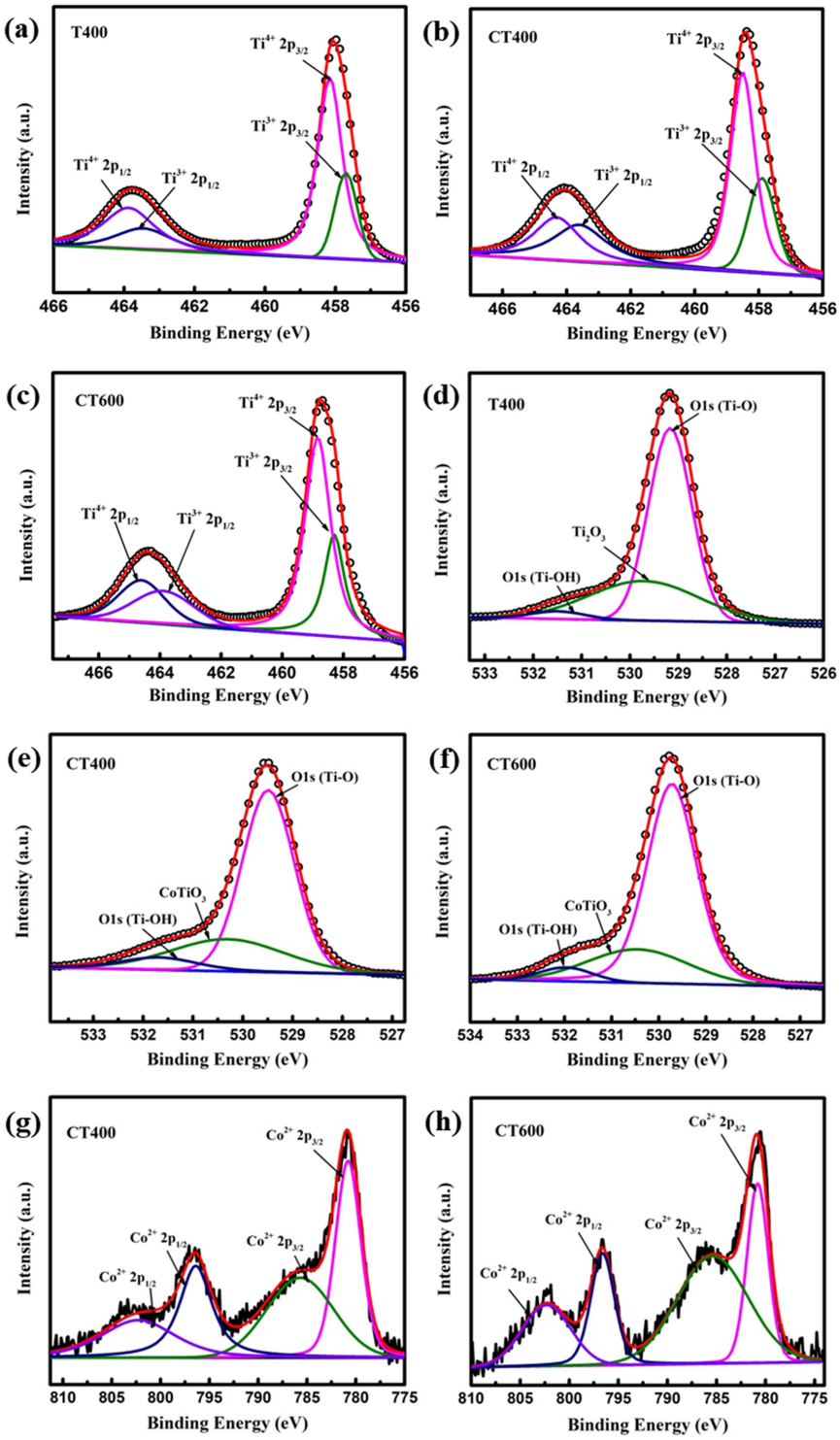

Figure 3.12. XPS peak fitting: Ti 2p spectrum of (a) T400, (b) CT400 and (c) CT600. O1s spectra of (d) T400, (e) CT400 and (f) CT600. Co 2p spectra of (g) CT400 and (h) CT600.

The broad O 1s spectra were deconvoluted into three peaks with BE positions of 529.2, 529.7, and 531.5 eV for T400 (Figure 3.12(d)); and 529.4, 530.3, and 531.7 eV for CT400 (Figure 3.12(e)); and 529.7, 530.4, and 532.0 eV for CT600 (Figure 3.12(f)). The well-fitted peaks at 529.7, 530.3, and 530.4 eV in T400, CT400, and CT600, respectively, are associated with the formation of Ti_2O_3 and $CoTiO_3$ in the matrix [44]. The slight reduction in the peak area of Ti_2O_3 in CT400 and CT600 suggests the formation of $CoTiO_3$.

The well-resolved Co 2p spectra of cobalt-doped CT400 and CT600 are shown in Figure 3.11(d). The XPS peaks at 780.7 and 796.4 eV, in CT400, are ascribed to the Co $2p_{3/2}$ and Co $2p_{1/2}$ core level transitions, respectively. Strong satellite peaks at 785.7 and 802.2 eV reveal the presence of a high spin Co^{2+} state in the TiO_2 matrix and the formation of mixed metal oxides ($CoTiO_3$) [40]. In CT600, the core level and satellite peaks are located at BE 780.8 (Co $2p_{3/2}$), 785.4 (satellite), 796.6 (Co $2p_{1/2}$), and 802.3 eV (satellite). The deconvoluted Co 2p spectra of CT400 and CT600 are shown in Figures 3.12(g) and 3.12(h). In CT600, the areas of the satellite peaks at 785.4 and 802.3 eV were larger than those in CT400 by ~74% and ~55%, respectively.

Table 3.2. XPS peak positions and areas of Ti 2p, Ti O1s, and Co 2p for T400, CT400 and CT600 photocatalysts.

Catalyst	Peak position (eV)	Area under the curve (a.u.)
T400	457.7 (**Ti^{3+} $2p_{3/2}$**)	18076.5
	458.2 (**Ti^{4+} $2p_{3/2}$**)	55467.9
	463.5 (**Ti^{3+} $2p_{1/2}$**)	13577.4
	464.0 (**Ti^{4+} $2p_{1/2}$**)	26763.6
CT400	457.8 (**Ti^{3+} $2p_{3/2}$**)	19331.6
	458.5 (**Ti^{4+} $2p_{3/2}$**)	42997.2
	463.6 (**Ti^{3+} $2p_{1/2}$**)	20028.3
	464.3 (**Ti^{4+} $2p_{1/2}$**)	19147.3
CT600	458.2 (**Ti^{3+} $2p_{3/2}$**)	21794.3
	458.8 (**Ti^{4+} $2p_{3/2}$**)	49685.8
	464.0 (**Ti^{3+} $2p_{1/2}$**)	15228.0
	464.6 (**Ti^{4+} $2p_{1/2}$**)	16385.2
T400	529.2 (**Ti-O**)	60501.36
	529.7 (**Ti_2O_3**)	31703.28
	531.5 (**Ti-OH**)	3007.993

CT400	529.4 (**Ti-O**)	57373.2
	530.3 (**$CoTiO_3$**)	23096.4
	531.7 (**Ti-OH**)	6587.84
CT600	529.7 (**Ti-O**)	66089
	530.4 (**$CoTiO_3$**)	20218.04
	532.0 (**Ti-OH**)	4384.933
CT400	780.7 (**Co^{2+} $2p_{3/2}$**)	22518.12
	785.7 (**satellite**)	19910.5
	796.4 (**Co^{2+} $2p_{1/2}$**)	15415.83
	802.2 (**satellite**)	7505.429
CT600	780.8 (**Co^{2+} $2p_{3/2}$**)	20977.9
	785.4 (**satellite**)	34755.62
	796.6 (**Co^{2+} $2p_{1/2}$**)	15589.91
	802.3 (**satellite**)	11682.63

3.3.7. Kinetic study for degradation of MB

Figure 3.13(a) shows the degradation trend of MB from 0 to 90 min using the synthesized photocatalysts under visible light illumination. For reference, control experiments were performed with fresh MB and pristine TiO_2. The degradation of MB was confirmed from the absorbance spectra of the reaction solution. Among the photocatalysts, CT600 exhibited the most rapid degradation. The reduction in MB concentration was ~7%, 56%, 97%, and 31% for T400, CT400, CT600, and CT700, respectively. The optical density spectra corresponding to MB dye degradation are displayed in Figure 3.14(a-d). These results indicate that maximum photocatalytic efficiency was achieved at a calcination temperature of 600 ºC. This is attributed to the mixed phase of TiO_2 at 600 ºC, where the homojunction between anatase and rutile enhances interfacial charge carrier transfer, and consequently minimizes the recombination rate [45].

The rate constant (k) of MB degradation was obtained from the linear fitting of $\ln(C/C_o)$-Time plot, displayed in Figure 3.13(b). CT600 photocatalyst shows ~42 times higher degradation rate than pristine TiO_2 (T400). This enhancement in the activity can be ascribed to (i) intermediate energy states due to Co^{2+} doping (bandgap reduction), (ii) homojunction between the anatase and rutile phase, and (iii) heterojunction between TiO_2 and $CoTiO_3$.

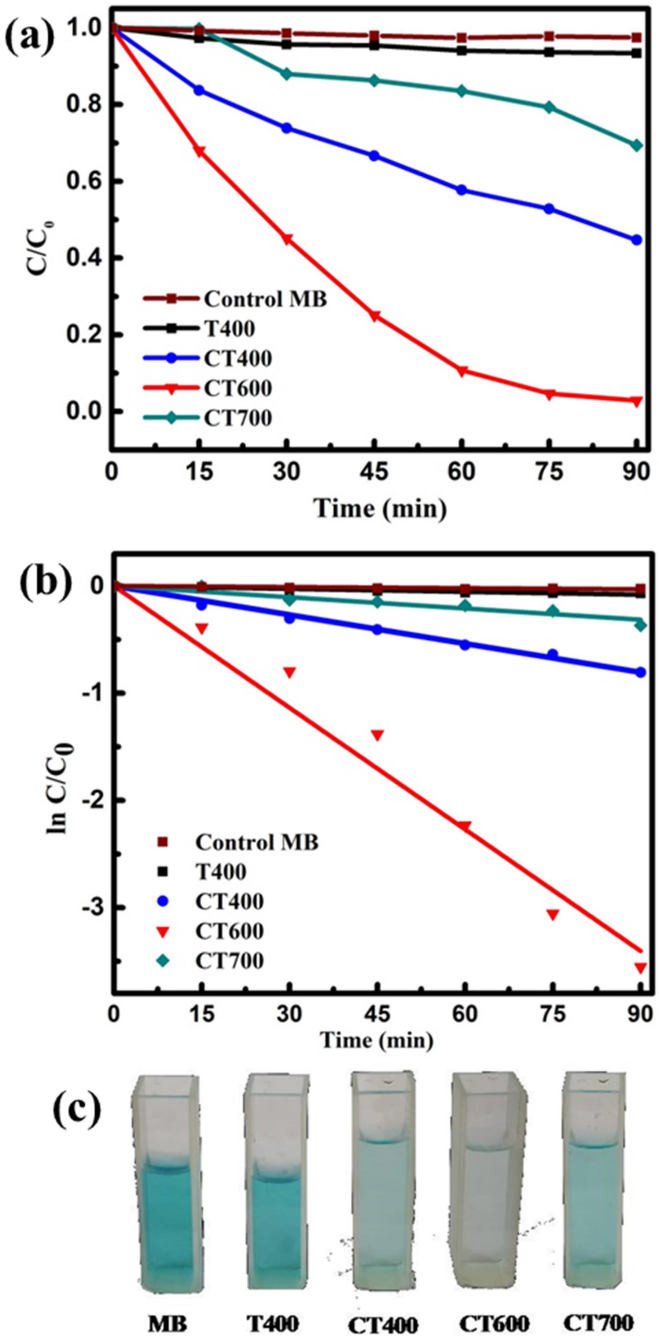

Figure 3.13. (a) Photocatalytic degradation profile (C/C_o vs. time) of MB under visible light (0 to 90 min) using T400, CT400, CT600, and CT700 photocatalysts. (b) ln (C/C_o) vs. time plot to measure the rate constant, (c) Optical images of MB degradation using T400, CT400, CT600, and CT700 photocatalysts, after visible light exposure for 90 min.

Table 3.3 displays the rate constant of MB degradation using various photocatalysts. A slight improvement in the photocatalytic activity of CT400 and CT700 compared to pure TiO_2 was observed, which could be ascribed to the light absorption due to $Co^{2+} \rightarrow Ti^{4+}$ charge transfer bands [26, 46]. The absence of homojunction in CT400 and CT700 accounts for lower degradation rate. The optical images of MB degradation of T400, CT400, CT600, and CT700 photocatalysts are shown in Figure 3.13(c).

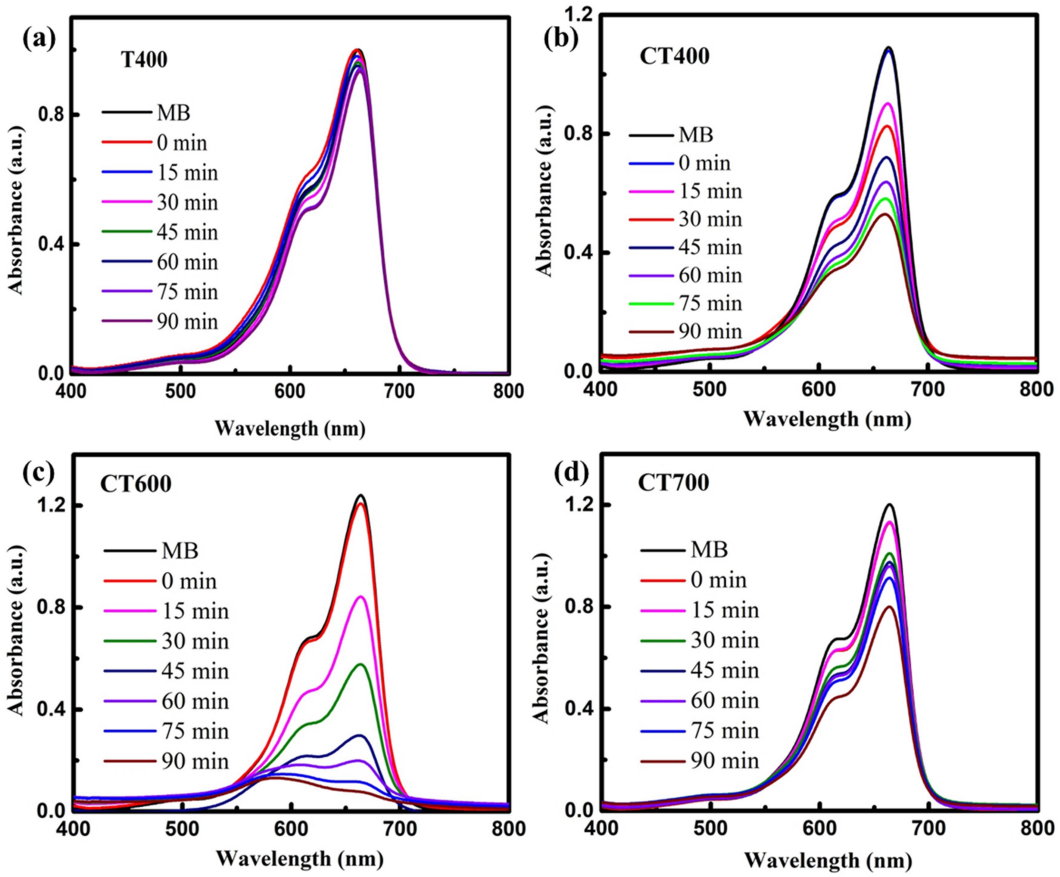

Figure 3.14. Absorption spectra of MB degradation with time using (a) T400, (b) CT400, (c) CT600, and (d) CT700. The maximum absorption at wavelength 664 nm was recorded. About 97% degradation of MB by Co-TiO_2/$CoTiO_3$ photocatalyst (CT600) in 90 min was observed.

Figure 3.15(a) illustrates the degradation of MB with illumination time (C/C_o vs. Time) for the T600 and T700 photocatalysts, and the corresponding rate constants are determined as shown in Figure 3.15(b). The existence of mixed polymorphs in T600 (as

confirmed by XRD analysis, Figure 3.3) leads to a slight enhancement (~1.2 times) in photocatalytic activity compared with T700 photocatalyst.

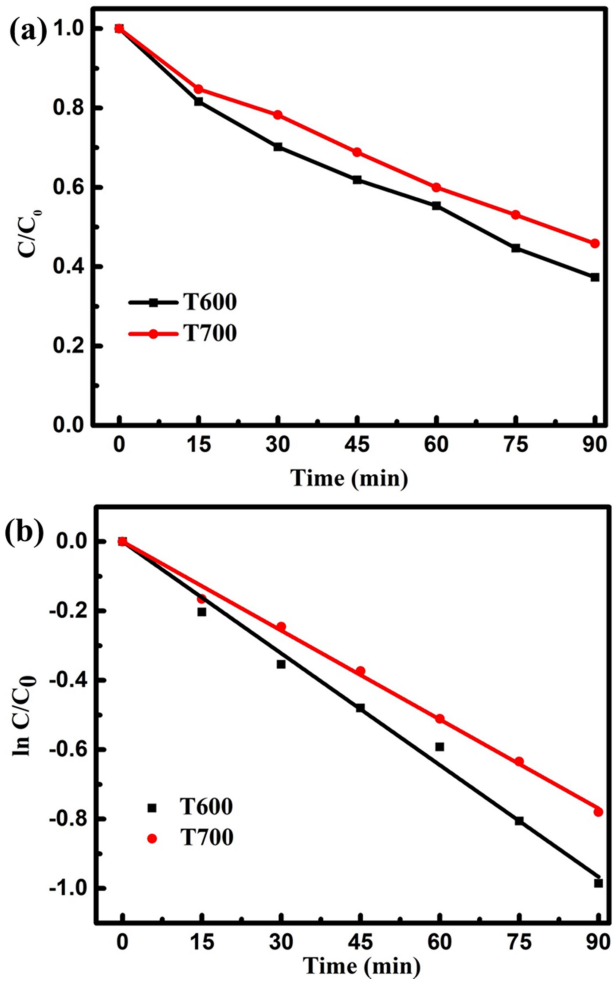

Figure 3.15. (a) Photocatalytic degradation profile (C/C_o vs. time) of MB using T600 and T700 and (b) ln C/C_o vs. time plot to measure the rate constant.

Table 3.3. Rate constant of MB degradation using various photocatalyst.

Catalyst	Rate constant (k) min^{-1}
T400	0.0009
CT400	0.0089
T600	0.01
CT600	0.0378

T700	0.0085
CT700	0.0035

3.3.8. Photocatalytic mechanism and schematic representation

The proposed photocatalytic mechanism of Co-TiO_2/$CoTiO_3$ (CT600) photocatalyst is illustrated in Figures 3.16(a) and 3.16(b). The photogenerated charge-carrier transfer occurs through interfacial junctions, comprising a Type I (straddling) heterojunction between TiO_2 and $CoTiO_3$ and Type II (staggered) homojunction between the anatase and rutile phases. The bandgap reduction of TiO_2 after Co doping arises from the formation of impurity states near the upper edge of the valence band (VB). Two possible heterojunction configurations are proposed: (a) $CoTiO_3$ with rutile-anatase and (b) $CoTiO_3$ with anatase-rutile sites of TiO_2, as shown in Figures 3.16(a) and 3.16(b).

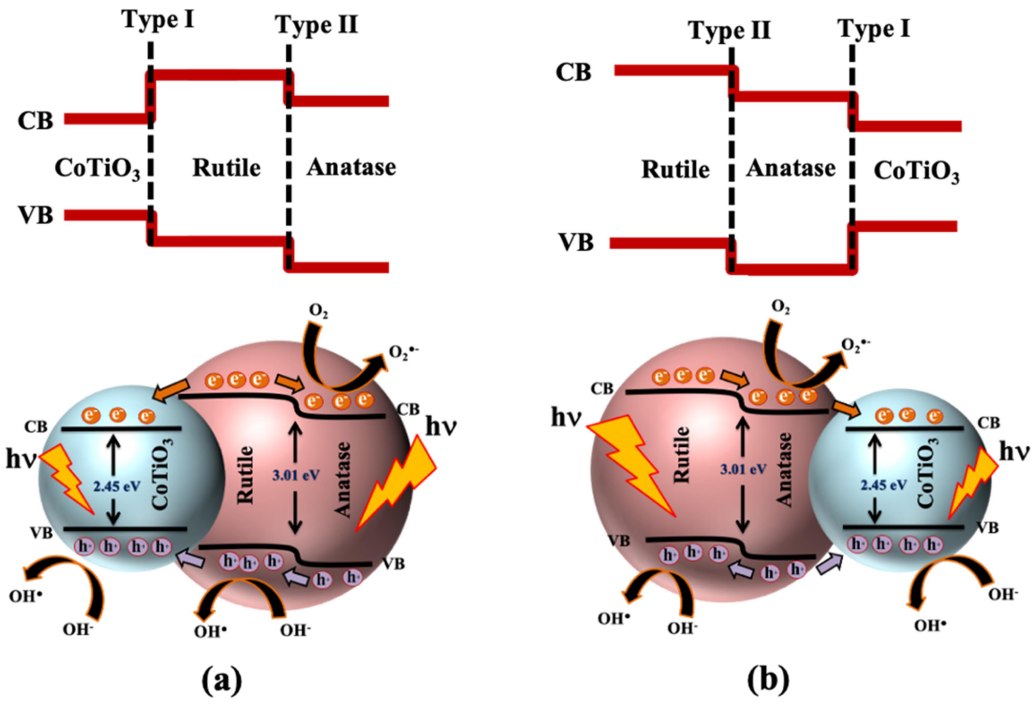

Figure 3.16. Photocatalytic mechanism of Co-TiO_2/$CoTiO_3$ (CT600) photocatalyst. Interfacial junctions between (a) $CoTiO_3$-rutile-anatase phase and (b) $CoTiO_3$-anatase-rutile phase of TiO_2.

In the first case, photoexcited electrons in the rutile phase readily migrate to the energetically lower conduction bands (CB) of anatase and $CoTiO_3$. Likewise, holes move from the valence band (VB) of anatase to rutile and subsequently to the VB of $CoTiO_3$. In the latter case, the photogenerated electrons migrate from the rutile phase to the CB of anatase and eventually to $CoTiO_3$, while holes generated in the VB of anatase transfer to the VB of $CoTiO_3$ and rutile phase. The localized electric field at the interface accelerates the charge-carrier transfer between the anatase-rutile homojunction and the $TiO_2/CoTiO_3$ heterojunction, thereby minimizing electron-hole recombination and ensuring the availability of charge carriers for photocatalytic reactions [7].

3.4. Summary

The interfacial junction between anatase-rutile TiO_2 homojunction and $CoTiO_3$ heterojunction was tailored by employing a facile and cost-effective approach. The bandgap of TiO_2 was reduced by Co^{2+} ion substitution and also increased surface oxygen vacancies that enhanced the photocatalytic reaction. The CT600 photocatalyst exhibited 97% degradation of MB dye within 90 min, which was 42-fold higher than that of pristine TiO_2. The enhanced photocatalytic performance of CT600 can be attributed to two major aspects: strong absorption across the visible light range and swift separation of charge carrier via homo- and heterojunctions in the Co-$TiO_2/CoTiO_3$. Importantly, this photocatalyst can effectively degrade MB in polluted water sources in a cost-effective and eco-friendly manner. The work presented in this chapter addresses two key objectives of the thesis: (i) fabricating a multi-junction photocatalytic system to enhance performance, and (ii) developing a viable photocatalyst through strategic bandgap engineering and surface modification. This material offers application for removal of water pollutants under natural solar light and represents a step forward toward sustainable water resources. Additionally, CT600 may also find application in water splitting for hydrogen production and as an electrode material in fuel cells.

References

1. C.H. Nguyen, C.C. Fu, R.S. Juang, Degradation of methylene blue and methyl orange by palladium-doped TiO_2 photocatalysis for water reuse: Efficiency and degradation pathways, J. Clean. Prod. 202 (2018) 413-427.

2. W.C. Oh, J.S. Bae, Preparation of Fe-ACF/TiO_2 Composites and their Photocatalytic Degradation of Waste Water, J. Korean Ceram. Soc. 45 (2008) 667-674.
3. H. Song, G. Zhou, C. Wang, X. Jiang, C. Wu, T. Li, Synthesis and photocatalytic activity of nanocrystalline TiO_2 co-doped with nitrogen and cobalt (II), Res. Chem. Intermed. 39 (2013) 747-758.
4. C. Liu, F. Wang, S. Zhu, Y. Xu, Q. Liang, Z. Chen, Controlled charge-dynamics in cobalt-doped TiO_2 nanowire photoanodes for enhanced photoelectrochemical water splitting, J. Colloid Interface Sci. 530 (2018) 403-411.
5. E.A. Mragui, O. Zegaoui, J.C.E. da Silva, Elucidation of the photocatalytic degradation mechanism of an azo dye under visible light in the presence of cobalt doped TiO_2 nanomaterials, Chemosphere 266 (2021) 128931.
6. Q. Chen, H. Shi, W. Shi, Y. Xu, D. Wu, Enhanced visible photocatalytic activity of titania–silica photocatalysts: effect of carbon and silver doping, Catal. Sci. Technol. 2 (2012) 1213-1220.
7. R. Zhou, S. Yang, E. Tao, L. Liu, J. Qian, The defect is perfect: MoS_2/TiO_2 modified with unsaturated Mo vacancies to construct Z-scheme heterojunction & improve mobility of e, J. Clean. Prod. 337 (2022) 130511.
8. N. Hellen, H. Park, K.N. Kim, Characterization of ZnO/TiO_2 nanocomposites prepared via the sol-gel method, J. Korean Ceram. Soc. 55 (2018) 140-144.
9. X.X. Zhang, Y.G. Xiao, S.S. Cao, Z.L. Yin, Z.Q. Liu, Ternary TiO_2@Bi_2O_3@ TiO_2 hollow photocatalyst drives robust visible-light photocatalytic performance and excellent recyclability, J. Clean. Prod. 352 (2022) 131560.
10. T. Han, Y. Chen, G. Tian, J.Q. Wang, Z. Ren, W. Zhou, H. Fu, Hierarchical $FeTiO_3$-TiO_2 hollow spheres for efficient simulated sunlight-driven water oxidation, Nanoscale 7 (2015) 15924-15934.
11. L. Liu, P. Li, B. Adisak, S. Ouyang, N. Umezawa, J. Ye, R. Kodiyath, T. Tanabe, G.V. Ramesh, S. Ueda, H. Abe, Gold photosensitized $SrTiO_3$ for visible-light water oxidation induced by Au interband transitions, J. Mater. Chem. A 2 (2014) 9875-9882.

12. G. Liu, L. Ma, L.C. Yin, G. Wan, H. Zhu, C. Zhen, Y. Yang, Y. Liang, J. Tan, H.M. Cheng, Selective chemical epitaxial growth of TiO_2 islands on ferroelectric $PbTiO_3$ crystals to boost photocatalytic activity, Joule 2 (2018) 1095-1107.
13. M. Enhessari, A. Parviz, K. Ozaee, E. Karamali, Magnetic properties and heat capacity of $CoTiO_3$ nanopowders prepared by stearic acid gel method, J. Exp. Nanosci. 5 (2010) 61-68.
14. M.C. Sekhar, B.P. Reddy, B.P. Prakash, S. Park, Effects of annealing temperature on phase transformation of $CoTiO_3$ nanoparticles and on their structural, optical, and magnetic properties, J. Supercond. Nov. Magn. 33 (2020) 407-415.
15. D. Cui, Y. Li, Y. Chen, Y. Li, Z. Hai, H. Xu, C. Xue, Synthesis of $CoTiO_3$ nanoparticles with enhanced photocatalytic degradation, Micro Nano Lett. 14 (2019) 840-844.
16. Y. Qu, W. Zhou, H. Fu, Porous cobalt titanate nanorod: a new candidate for visible light-driven photocatalytic water oxidation, ChemCatChem 6 (2014) 265-270.
17. B. Lin, S. Li, Y. Peng, Z. Chen, X. Wang, MOF-derived core/shell C-TiO_2/$CoTiO_3$ type II heterojunction for efficient photocatalytic removal of antibiotics, J. Hazard. Mater. 406 (2021) 124675.
18. A. Noypha, Y. Areerob, S. Chanthai, P. Nuengmatcha, Fe_2O_3-graphene anchored Ag nanocomposite catalyst for enhanced sonocatalytic degradation of methylene blue, J. Korean Cream. Soc. 58 (2021) 297-306.
19. G. Palanisamy, K. Bhuvaneswari, G. Bharathi, T. Pazhanivel, A.N. Grace, S.K.K. Pasha, Construction of magnetically recoverable ZnS-WO_3-$CoFe_2O_4$ nanohybrid enriched photocatalyst for the degradation of MB dye under visible light irradiation, Chemosphere 273 (2021) 129687.
20. R. Praharaj, S. Mishra, T.R. Rautray, The structural and bioactive behaviour of strontium-doped titanium dioxide nanorods, J. Korean Ceram. Soc. 57 (2020) 271-280.
21. B. Choudhury, A. Choudhury, Local structure modification and phase transformation of TiO_2 nanoparticles initiated by oxygen defects, grain size, and annealing temperature, Int. Nano Lett. 3 (2013) 1-9.

22. R.S. Dubey, Temperature-dependent phase transformation of TiO_2 nanoparticles synthesized by sol-gel method, Mater. Lett. 215 (2018) 312-317.
23. Y. H. Zhang, A. Reller, Phase transformation and grain growth of doped nanosized titania, Mater. Sci. Eng. C 19 (2002) 323–326
24. X. Z. Ding, X. H. Liu, Correlation between anatase-to-rutile transformation and grain growth in nanocrystalline titania powders, J. Mater. Res. 13 (1998) 2556–2559.
25. B. Anitha, M.A. Khadar, A. Banerjee, Paramagnetic behavior of Co doped TiO_2 nanocrystals controlled by self-purification mechanism, J. Solid State Chem. 239 (2016) 237-245.
26. R. Ye, H. Fang, Y.Z. Zheng, N. Li, Y. Wang, X. Tao, Fabrication of $CoTiO_3$/g-C_3N_4 hybrid photocatalysts with enhanced H_2 evolution: Z-scheme photocatalytic mechanism insight, ACS Appl. Mater. Interfaces 8 (2016) 13879-13889.
27. M. Borah, D. Mohanta, Structural and optoelectronic properties of Eu^{2+}-doped nanoscale barium titanates of pseudo-cubic form, J. Appl. Phys. 112 (2012) 124321.
28. J. T-Thienprasert, S. Klaithong, A. Niltharach, A. Worayingyong, S. Na-Phattalung, S. Limpijumnong, Local structures of cobalt in Co-doped TiO_2 by synchrotron x-ray absorption near edge structures, Curr. Appl. Phys. 11 (2011) S279-S284.
29. K. Wangkawong, S. Suntalelat, D. Tantraviwat, B. Inceesungvorn, Novel $CoTiO_3/Ag_3VO_4$ composite: synthesis, characterization and visible-light-driven photocatalytic activity, Mater. Lett. 133 (2014) 119-122.
30. D. Konwar, P. Basumatary, S.P. Woo, Y. Lee, Y.S. Yoon, Enhanced performance for proton conducting fuel cells at low temperature, Electrochim. Acta 290 (2018) 142-149.
31. G. Yang, D. Gao, J. Zhang, J. Zhang, Z. Shi, D. Xue, Evidence of vacancy-induced room temperature ferromagnetism in amorphous and crystalline Al_2O_3 nanoparticles, J. Phys. Chem. C 115 (2011) 16814-16818.
32. G. Yang, Z. Jiang, H. Shi, T. Xiao, Z. Yan, Preparation of highly visible-light active N-doped TiO_2 photocatalyst, J. Mater. Chem. 20 (2010) 5301-5309.

33. L.T. Tseng, X. Luo, T.T. Tan, S, Li, J. Yi, Doping concentration dependence of microstructure and magnetic behaviours in Co-doped TiO_2 nanorods, Nanoscale Res. Lett. 9 (2014) 1-10.
34. L. Chetibi, T. Busko, N.P. Kulish, D. Hamana, S. Chaieb, S. Achour, Photoluminescence properties of TiO_2 nanofibers, J. Nanoparticle Res. 19 (2017) 1-9.
35. S. Mathew, T. Benoy, P.P. Rakesh, M. Hari, T.M. Libish, P. Radhakrishnan, Mathew, S., Thomas Benoy, P.P. Rakesh, Misha Hari, T.M. Libish, P. Radhakrishnan, V.P.N. Nampoori, C.P.G. Vallabhan, UV-visible photoluminescence of TiO_2 nanoparticles prepared by hydrothermal method, J. Fluoresc. 22 (2012) 1563-1569.
36. M. Sreemany, T.B. Ghosh, B.C. Pai, M. Chakraborty, XPS studies on the oxidation behavior of SiC particles, Mater. Res. Bull. 33 (1998) 189-198.
37. Z. Wang, C. Yang, T. Lin, H. Yin, P. Chen, D. Wan, F. Xu, F. Huang, J. Lin, X. Xie, M. Jiang, H-doped black titania with very high solar absorption and excellent photocatalysis enhanced by localized surface plasmon resonance, Adv. Funct. Mater. 23 (2013) 5444-5450.
38. K. Wang, T. Peng, Z. Wang, H. Wang, X. Chen, W. Dai, X. Fu, Correlation between the H_2 response and its oxidation over TiO_2 and N doped TiO_2 under UV irradiation induced by Fermi level, Appl. Catal. B: Environ. 250 (2019) 89-98.
39. Y. Matsumoto, M. Katayama, T. Abe, T. Ohsawa, I. Ohkubo, H. Kumigashira, M. Oshima, H. Koinuma, Chemical trend of Fermi-level shift in transition metal-doped TiO_2 films, J. Ceram. Soc. Japan 118 (2010) 993-996.
40. B. Bharti, S. Kumar, H.N. Lee, R. Kumar, Formation of oxygen vacancies and Ti^{3+} state in TiO_2 thin film and enhanced optical properties by air plasma treatment, Sci. Rep. 6 (2016) 1-12.
41. R. Sanjines, H. Tang, H. Berger, F. Gozzo, G. Margaritondo, F. Levy, Electronic structure of anatase TiO_2 oxide, J. Appl. Phys. 75 (1994) 2945-2951.
42. G. Yang, W. Yan, J. Wang, H. Yang, Fabrication and characterization of $CoTiO_3$ nanofibers by sol-gel assisted electrospinning, Mater. Lett. 122 (2014) 117-120.
43. Y. Yang, P. Gao, X. Ren, L. Sha, P. Yang, J. Zhang, Y. Chen, L. Yang, Massive Ti^{3+} self-doped by the injected electrons from external Pt and the efficient

photocatalytic hydrogen production under visible-Light, Appl. Cat. B: Environ. 218 (2017) 751-757.

44. J.Y. Tai, K.H. Leong, P. Saravanan, A.A. Aziz, L.C. Sim, Dopant-free oxygen-rich titanium dioxide: LED light-induced photocatalysis and mechanism insight, J. Mater. Sci. 52 (2017) 11630-11642.
45. R.I. Bickley, T. Gonzalez-Carreno, J.S. Lees, L. Palmisano, R.J. Tilley, A structural investigation of titanium dioxide photocatalysts, J. Solid State Chem. 92 (1991) 178-190.
46. L. Samet, J.B. Nasseur, R. Chtourou, K. March, O. Stephan, Heat treatment effect on the physical properties of cobalt doped TiO_2 sol–gel materials, Mater. Charact. 85 (2013) 1-12.